Investigating intracranial tumour growth patterns with multiparametric MRI incorporating Gd-DTPA and USPIO-enhanced imaging

Jessica K.R. Boult[1], Marco Borri[1,2], Alexa Jury[3,4], Sergey Popov[3,4], Gary Box[4], Lara Perryman[3,4], Suzanne A. Eccles[4], Chris Jones[3,4], Simon P. Robinson[1]

[1]Division of Radiotherapy and Imaging, The Institute of Cancer Research, London, UK.
[2]Royal Marsden NHS Foundation Trust, London, Surrey, UK
[3]Division of Molecular Pathology, The Institute of Cancer Research, London, UK.
[4]Division of Cancer Therapeutics, The Institute of Cancer Research, London, UK.

Corresponding author: Dr Jessica Boult
Division of Radiotherapy and Imaging
The Institute of Cancer Research,
London
SM2 5NG, UK

Telephone: +44 (0)208 722 4699
Email: Jessica.Boult@icr.ac.uk

Running Title: Dual contrast enhanced MRI of intracranial tumours

Keywords: Magnetic resonance imaging; gadolinium-enhanced MRI; USPIO; dual-contrast MRI; high grade glioma; breast metastases

Word Count: 5364

Grant Support

We acknowledge the CRUK and EPSRC support to the Cancer Imaging Centre at The Institute of Cancer Research and The Royal Marsden Hospital in association with the MRC and Department of Health (England) (C1060/A10334, C1090/A16464), CRUK funding to the Cancer Therapeutics Unit (C309/A11566), and NHS funding to the NIHR Biomedical Research Centre at The Royal Marsden and the ICR.

Abbreviations

ADC	apparent diffusion coefficient
ARRIVE	animal research: reporting *in vivo* experiments
BBB	blood brain barrier
DW-MRI	diffusion-weighted MRI
EPI	echo-planar imaging
fBV	fractional blood volume
GBM	glioblastoma (multiforme)
H&E	haematoxylin and eosin
MGE	multi gradient-recalled echo
STR	short tandem repeat
IR-trueFISP	inversion recovery true fast imaging with steady-state precession
USPIO	ultrasmall superparamagnetic iron oxide
VEGF	vascular endothelial growth factor

Abstract

High grade and metastatic brain tumours exhibit considerable spatial variations in proliferation, angiogenesis, invasion, necrosis and oedema. Vascular heterogeneity arising from vascular co-option in regions of invasive growth, in which the blood brain barrier remains intact, and neoangiogenesis is a major challenge faced in the assessment of brain tumours by conventional MRI.

A multiparametric MRI approach, incorporating native measurements and both Gd-DTPA (Magnevist) and ultrasmall superparamagnetic iron oxide (USPIO, P904)-enhanced imaging was used, in combination with histogram and unsupervised cluster analysis using a k-means algorithm, to examine the spatial distribution of vascular parameters, water diffusion characteristics and invasion in intracranially propagated rat RG2 gliomas and human MDA-MB-231 LM2-4 breast adenocarcinomas in mice.

Both tumour models presented with higher ΔR_1 (the change in transverse relaxation rate R_1 induced by Gd-DTPA), fractional blood volume (fBV) and apparent diffusion coefficient (ADC) than uninvolved regions of the brain. MDA-MB-231 LM2-4 tumours were less densely cellular than RG2 tumours and exhibited substantial local invasion, associated with oedema, whereas invasion in RG2 tumours was minimal. These additional features were reflected in the more heterogeneous appearance of MDA-MB-231 LM2-4 tumours on T_2-weighted images and maps of functional MRI parameters.

Unsupervised cluster analysis separated subregions with distinct functional properties; areas with a low fBV and relatively impermeable blood vessels (low ΔR_1) were predominantly located at the tumour margins, regions of MDA-MB-231 LM2-4 tumours with relatively high levels of water diffusion and low vascular permeability and/or fBV corresponded to histologically-identified regions of invasion and oedema, and areas of mismatch between vascular permeability and blood volume were identified.

We demonstrate that dual contrast MRI and evaluation of tissue diffusion properties, coupled with cluster analysis, allows for the assessment of heterogeneity within invasive brain tumours and the designation of functionally diverse subregions that may provide more informative predictive biomarkers.

Introduction

The effective treatment of brain tumours is an unmet and urgent clinical need. Five year survival for patients with grade IV glioma (glioblastoma, GBM) is only 5% (1); while patients with low-grade gliomas have a better prognosis, there is, as yet, no assured cure using conventional therapies. Patients with brain metastases, which affect approximately 8-10% of cancer patients, and approximately 30% of patients with breast cancer, have a similarly poor prognosis (2,3). High grade and metastatic brain tumours exhibit considerable spatial heterogeneity in gene expression and biochemistry, resulting in regional differences in tumour cell and microvascular proliferation, angiogenesis, necrosis and invasion. Diffuse infiltration of tumour cells in the neuropil, the dense network of interwoven neuronal and glial cell processes, is a characteristic of both low and high grade brain tumours (4), and whose clinical management is one of the greatest challenges facing neuro-oncologists and radiologists treating patients with brain tumours.

Imaging biomarkers for the assessment of tumour pathophysiology and response to therapeutics are now widespread in the clinic and diagnostic imaging is an essential tool in the treatment stratification of patients with brain tumours. Magnetic resonance imaging (MRI) enables the visualisation of detailed anatomical features with high resolution due to its exquisite soft tissue image contrast (5) and is therefore the imaging methodology of choice for defining brain tumour anatomy and delineating tumours. Advanced MRI also provides a means of defining quantitative biomarkers to inform on biologically relevant structure-function relationships in tumours, enabling an understanding of the behaviour and heterogeneous distribution of such associations (6). There is a pressing need for refined MRI strategies and quantitative biomarkers to accurately interrogate specific growth patterns associated with infiltrative intracerebral tumours.

Conventional gadolinium-enhanced MRI, which is used extensively for diagnosis and staging, and in early stage clinical trials in solid tumours, relies upon the hyperpermeable nature of neoangiogenic tumour blood vessels. Infiltrating tumour cells in the brain obtain essential nutrients by co-opting the existing vasculature, leaving the blood brain barrier (BBB) intact, and consequently making appropriate delineation of infiltrative brain tumours problematic. Macromolecular ultrasmall superparamagnetic iron oxide (USPIO) particles, which remain within the vasculature over the duration of the MR imaging timeframe, have been used extensively pre-clinically to delineate blood vessels and to provide estimates of fractional tumour blood volume and vessel calibre (7-9). USPIO-enhanced MRI, alone or in combination with gadolinium-enhanced MRI, may therefore enable delineation of vessels within glioma regions with an intact BBB within co-optive, infiltrative areas.

We hypothesised that functional MRI, incorporating assessment of vascular parameters and diffusion characteristics, can report on heterogeneity within infiltrative brain tumours and inform on functionally diverse habitats. We employed a multiparametric MRI approach incorporating native measurements and both Gd-DTPA- and USPIO-enhanced imaging, and assessed the data using histogram and unsupervised cluster analysis, to examine the spatial distribution of vascular permeability and volume, diffusion characteristics and invasion in RG2 and MDA-MB-231 LM2-4 intracranial tumours *in vivo*.

Materials and Methods

Cell Culture

RG2 rat glioma cells that stably express pGL4.50[luc2/CMV/hygro] (ATCC: Kind gift from Dr. D. Crichton, Cancer Research Technology, The Beatson Institute for Cancer Research, Glasgow. March 2010) and luciferase-expressing MDA-MB-231 LM2-4 highly malignant human triple negative breast adenocarcinoma cells derived from a lung metastasis from an orthotopic MDA-MB-231 tumour (10) (provided by Dr. R. Kerbel, University of Toronto, Canada) were maintained in Dulbecco's Modified Eagle's Medium supplemented with 10% (v/v) foetal bovine serum (all Invitrogen, Life Technologies, Paisley, UK). Both cell lines tested negative for mycoplasma infection, and MDA-MB-231 LM2-4 cells were authenticated by short tandem repeat (STR) profiling, at the time of tumour propagation.

Animals and Tumours

All experiments were performed in accordance with the local ethical review panel, the UK Home Office Animals (Scientific Procedures) Act 1986, the United Kingdom National Cancer Research Institute guidelines for the welfare of animals in cancer research (11) and the ARRIVE (animal research: reporting *in vivo* experiments) guidelines (12). RG2 or MDA-MB-231 LM2-4 cells ($5x10^3$) were implanted supratentorially in the brains of 6 week old female athymic (NCr-*Foxn1*^{nu}) mice (Charles River Ltd, Margate, UK), as previously described (13). A total of thirteen RG2 and fourteen MDA-MB-231 LM2-4 tumour bearing mice were used in this study.

Bioluminescence Imaging

Tumour establishment and growth was monitored by bioluminescence imaging using a Xenogen IVIS® 200 system coupled with LivingImage software (Caliper Life Sciences, Runcorn, UK). The luciferase substrate luciferin (150mg/kg, Caliper Life Sciences) was administered intraperitoneally

10 minutes before imaging. Total photon flux was established for automatically drawn regions of interest (ROIs) at a constant threshold.

Magnetic Resonance Imaging

^{1}H magnetic resonance imaging (MRI) was performed on a 7T Bruker horizontal bore microimaging system (Ettlingen, Germany) using a 3cm birdcage coil and a 2.5cm x 2.5cm field of view. Anaesthesia was induced with a 10ml/kg intraperitoneal injection of fentanyl citrate (0.315mg/ml) plus fluanisone (10mg/ml (Hypnorm; Janssen Pharmaceutical Ltd. High Wycombe, UK)), midazolam (5mg/ml (Hypnovel; Roche, Burgess Hill, UK)), and sterile water (1:1:2). Both lateral tail veins were cannulated with a 27G butterfly catheter (Venisystems, Hospira, Royal Leamington Spa, UK) to enable the remote administration of Gd-DTPA (Magnevist™; Schering, Berlin, Germany; particle size <0.1nm) and USPIO particles (P904; Guerbet, Villepinte, France; particle size 25-30nm). Core body temperature was maintained by warm air blown through the magnet bore.

Magnetic field homogeneity was optimised by shimming over the entire brain using an automated shimming routine (FASTMAP). A morphological, 20-slice, fast, multi-slice RARE spin-echo sequence was first used for localisation of the tumour and measurement of tumour volume. Next, diffusion-weighted (DW) images were acquired using an echo-planar diffusion-weighted (EPI-DWI) sequence (T_R=1500ms, T_E=32ms, 10 b-values; b=0, 30, 60, 100, 150, 200, 300, 500, 750, 1000s/mm^2, 4 averages, 3x1mm slices). Subsequently, images were acquired from the same central slice using an inversion recovery (IR) true fast imaging with steady-state precession (trueFISP) sequence (T_E=1.2ms, T_R=2.4ms, scan T_R=10s, T_I=29-1930ms, 50 inversion times, 8 averages, matrix=128x128, 1x1mm slice, scan duration 10 minutes 40 seconds) prior to and 1 minute after administration of 0.1mmol/kg Gd-DTPA i.v. (Magnevist). Multi gradient-recalled echo (MGE) images (T_R=1000ms, T_E=6.2-31.1ms, 8 echoes, 2 averages, matrix=256x256, 9x1mm slices) were

acquired prior to and 2 minutes after intravenous administration of USPIO particles (150µmol Fe/kg, 8.38mg Fe/kg P904).

MRI Data Analysis

Parameter estimation was undertaken using a Bayesian maximum *a posteriori* algorithm, which took into account the Rician distribution of noise in magnitude MR data in order to provide unbiased parameter estimates (14,15). Estimates of the apparent diffusion coefficient (ADC, $x10^{-6}$ mm^2 s^{-1}) were determined from the EPI-DWI data. The dual relaxation rate sensitivity of the IR-trueFISP sequence was utilised to provide estimates of both the native longitudinal and transverse relaxation times, T_1 and T_2 (ms). The change in R_1 ($=1/T_1$, ΔR_1, s^{-1}) following delivery of Gd-DTPA was also evaluated. The transverse relaxation rate R_2* (s^{-1}) was quantified using the MGE data, and the USPIO-induced change in R_2* (ΔR_2*) was used to estimate fractional blood volume (fBV, %), using the following equation (7,16):

$$fBV = \frac{3}{4\pi}\frac{\Delta R_2 *}{\gamma \Delta \chi B_0}$$

Where $\Delta\chi$, the change in susceptibility induced by USPIO, was taken to equal 0.408 ppm, the Larmor frequency of protons (γ) taken to equal 4.26×10^7/s/T and the static magnetic field strength B_0 = 7T. The value of $\Delta\chi$ is valid for the dose of USPIO contrast agent used *in vivo* in mice (7). Pixels corresponding to a fBV exceeding 17% (the limit value for the linearity between ΔR_2* and fBV (17)) were excluded. All data were fitted on a pixel-by-pixel basis using in-house software (ImageView, developed in IDL, ITT Visual Information Systems, Boulder, CO, USA), and the median value of each parameter determined from a region of interest (ROI) that encompassed the whole tumour. Where possible, ROIs were also drawn over an uninvolved region of the brain in the contralateral hemisphere to the injection of cells, on an imaging slice containing tumour, and the same analyses performed as for tumour ROIs.

Cluster Analysis

Unsupervised cluster analysis was performed using in-house software developed in IDL. The K-means algorithm was employed to partition the ROIs into sub-regions of similar characteristics, defined in the two-dimensional (2D) feature space formed by the two parameters ΔR_1 and fBV, ΔR_1 and ADC, or fBV and ADC, and the three-dimensional (3D) feature space formed all three parameters (18). The optimal number of clusters for each dataset was determined using the cluster validation method described by Sugar and James (19).

Histological Analysis

Where possible, tumour bearing mice were administered with 15mg/kg of the perfusion marker Hoechst 33342 (Sigma-Aldrich, Poole, UK) intravenously through a lateral tail vein with the intact brain being rapidly excised one minute later, snap-frozen and stored in liquid nitrogen (20).

Hoechst 33342 fluorescence signals were recorded at 365nm from whole frozen brain sections (10μm thick, three per tumour) using a motorised scanning stage (Prior Scientific Instruments, Cambridge, UK) attached to a BX51 microscope (Olympus Optical, London, UK), driven by CellP (Soft Imaging System, Münster, Germany). In addition, images of the tumour region only were acquired.

The same sections were then stained with haematoxylin and eosin (H&E), and composite images were acquired using the same microscope system and co-ordinates under bright field illumination. These images were then used to draw tumour ROIs for analysis of the Hoechst 33342 data. Fluorescent particles were detected above a constant threshold, and the area of the tumour section with Hoechst 33342 fluorescence was determined and expressed as a percentage of the whole tumour area.

The brains from the remaining mice bearing intracranial RG2 or MDA-MB-231 LM2-4 tumours (n=5 and n=4, respectively) were formalin-fixed and paraffin-embedded and 5μm sections were cut.

Sections from two levels through each tumour were stained with H&E, and cellular density assessed by counting the number of nuclei in four square ROIs with a side length of 50µm, resulting in a total area assessed of 0.01mm^2 per field (200x magnification) (21). Three or more fields per section were assessed.

Statistical Analysis

Statistical analysis was performed using GraphPad Prism (GraphPad Software, Inc., La Jolla, CA, USA). Results are presented as the mean ± 1 standard error of the mean (s.e.m.), for imaging data the median value is taken for each tumour, and the cohort mean reported. Significance testing used Student's unpaired or paired t-tests, where appropriate, with a 5% confidence level. Frequency histograms were produced (data acquired from all slices in individual animals and from all the animals in the cohort combined), and the degree of skew and kurtosis, were assessed.

Results

A multiparametric MRI protocol, incorporating DW- and dual contrast enhanced MRI, was performed on mice bearing intracranially propagated rat RG2 glioma and human MDA-MB-231 LM2-4 breast adenocarcinoma tumours. MRI was carried out when the tumour total photon flux reached a previously established threshold for each model representing a volume of approximately 50mm^3 (mean MRI-derived volume; RG2 47±12mm^3, MDA-MB-231 LM2-4 53±7mm^3, 22±0.2 and 24±2.7 days post injection, respectively). Representative anatomical T_2-weighted images and parametric maps of ADC, native T_1 and T_2, ADC, ΔR_1 and fBV from each tumour model are shown in Figure 1a. The quantitative MRI data for tumour and uninvolved brain ROIs is summarised in Table 1.

RG2 tumours revealed a more homogeneous appearance on T_2-weighted MRI than MDA-MB-231 LM2-4 tumours. Whilst both tumour models demonstrated heterogeneity in parametric functional MRI maps, the degree of heterogeneity appeared greater in MDA-MB-231 LM2-4 tumours. ADC was higher in both tumours than in uninvolved brain regions of the same animals. Histogram analysis revealed similar shaped distributions of ADC values in both tumour types, but with a shift towards higher values in the MDA-MB-231 LM2-4 data, resulting in a significantly higher median ADC (Figure 1b). Intracranial MDA-MB-231 LM2-4 tumours also exhibited significantly longer median T_1 and T_2 relaxation times, compared with orthotopic RG2 xenografts.

Administration of Gd-DTPA increases the relaxation rate R_1 in areas of brain tumours where the vasculature is permeable, for example in areas where the blood brain barrier is disrupted. The change in the tumour R_1 (ΔR_1) following Gd-DTPA administration was significantly greater in MDA-MB-231 LM2-4 tumours than in RG2 tumours (Table 1). Insufficient ROIs could be drawn in uninvolved regions on the IR-trueFISP images in order to perform comparisons on paired

regions, but ΔR_1 in both tumour types was significantly higher than that determined from uninvolved regions of both RG2 and MDA-MB-231 LM2-4-bearing brains. The frequency distribution of the combined uninvolved ROI data shows that ΔR_1 values in these regions were spread over a narrower range at the lower end of the distribution of the tumour data, but there was no significant difference in skew or kurtosis between the individual ROI frequency distributions.

Fractional blood volume (fBV) was significantly higher in both tumour models than in uninvolved regions of the brains of the same animals, and was significantly lower in MDA-MB-231 LM2-4 tumours than RG2 tumours (Table 1). Frequency distributions revealed a lower occurrence of fBV values below approximately 7% in the tumour regions than the corresponding uninvolved regions of interest, a pattern seen to a lower extent between the MDA-MB-231 LM2-4 and RG2 tumours. The frequency distributions of ADC and fBV data in the uninvolved regions of mice bearing RG2 and MDA-MB-231 LM2-4 tumours were similarly shaped.

H&E staining revealed that tumours derived from MDA-MB-231 LM2-4 cells grew as partially well circumscribed masses with substantial local invasion, principally occurring along existing blood vessels (Figure 2a, open head arrow), but also through the brain parenchyma. Tumours derived from RG2 cells grew as well circumscribed masses with limited areas of local invasion typically presenting as small groups of tumour cells or finger-like projections a small distance from the tumour border (Figure 2a). RG2 tumour cellularity was homogeneous and dense, whereas MDA-MB-231 LM2-4 tumours presented with regions of sparse cell density and oedema (Figure 2a, closed head arrow). Quantitative analysis confirmed a significantly lower cellular density in MDA-MB-231 LM2-4 tumours (64±5 nuclei/0.01mm^2) compared with RG2 tumours (82± 3 nuclei/0.01mm^2; $p<0.05$). Hoechst 33342 perfused area was assessed and quantified in MDA-MB-231 LM2-4 and RG2 tumours (Figure 2b); no significant difference between the tumour types was observed. A positive and statistically significant correlation was determined between Hoechst

33342 perfused area and MRI derived fBV in the RG2 tumours with matched fBV and Hoechst 33342 data (n=4, r^2=0.93, $p<0.05$) but there was no significant relationship between fBV and Hoechst 33342 perfusion in the MDA-MB-231 LM2-4 tumours with matched data (n=5, r^2=0.30, $p>0.05$).

In order to assess the basis of the heterogeneity observed in intracranial tumours, particularly the more invasive MDA-MB-231 LM2-4, unsupervised cluster analysis was used to identify subregions with comparable functional parameters, and therefore similar biological properties, based on ΔR_1, fBV and ADC. When applied to complete fBV datasets, the method identified an 'outlier' cluster of high fBV voxels (Supplementary Figure S1a). In order to eliminate this cluster and optimise the utility of the cluster analysis, a threshold was applied to each dataset, defined as the value below which a data point had only a 5% probability of belonging to the 'outlier' cluster, yielding thresholds of 21.2% for RG2 and 19.7% for MDA-MB-231 LM2-4 tumours. These values are in good agreement with the 17% threshold previously applied and reported by Troprès *et al.* (17), based on the observation that there is no longer linearity between ΔR_2* and fBV above this value. Following this, the optimal number of clusters was then established as four for the 2D assessment of ΔR_1 and fBV in the RG2 tumours, and three for the 2D assessment of all pairs of parameters and the 3D assessment of ΔR_1, fBV and ADC together in MDA-MB-231 LM2-4 (19).

Voxel distribution partitioned with the optimal number of clusters, cluster analysis colour maps of a representative tumour slice, and associated H&E images are shown in Figure 3. Figure S1b shows 2D projections of the clustered 3D voxel distribution of all three parameters in MDA-MB-231 LM2-4, providing a 2D view of the distribution for each parameter pair. In the maps of ΔR_1 and fBV, red voxels indicative of areas with a low blood volume (low fBV) and relatively impermeable blood vessels (low ΔR_1), were predominantly located at the tumour margins. Yellow voxels originate from subregions with a low blood volume but high vascular permeability. In the MDA-

MB-231 LM2-4 tumours, all voxels with high fBV clustered together (blue voxels), irrespective of their relative vascular permeability, and were associated with the viable tumour mass. This cluster, driven by relatively high fBV, is also evident in cluster maps combining fBV with ADC and when the contributions from all three functional parameters are combined, although this is coupled with relatively high ΔR_1. In RG2 tumours, however, these high fBV voxels were divided between those with low (blue) and high vascular permeability (green), and were heterogeneously distributed throughout the tumours.

Cluster analysis maps of ΔR_1 and ADC in the MDA-MB-231 LM2-4 tumours revealed yellow voxels with relatively high levels of water diffusion and low vascular permeability, and which largely corresponded to histologically-identified areas of invasion, vascular co-option and clear evidence of oedema (Figure 3c, closed head arrow). This subregion was also identifiable on cluster analysis maps of ADC and fBV, where high ADC coincides with low fBV and is clearly identifiable on the 3D analysis incorporating all three parameters. Red voxels with low vascular permeability but relatively restricted diffusion were associated with areas of invasion without oedema (Figure 3c, open head arrow), as were voxels ascribed to the red cluster with low fBV and low ADC. Blue voxels with higher ΔR_1 and therefore higher vascular permeability, but with a range of ADC values, corresponded to the main dense cellular mass and largely corresponds to the red cluster in the three parameter maps corresponding to relatively low fBV, high ΔR_1 and low ADC and the yellow cluster in maps incorporating fBV and ΔR_1.

Discussion

High grade and metastatic brain tumours exhibit considerable spatial variations in proliferation, cellularity, angiogenesis, invasion, necrosis and oedema. Recent publications have highlighted the potential value of spatial analysis of brain tumours, combining multiple MRI parameters to segment tumour from healthy tissue and to establish regional variations within tumours (22-25). Amongst the greatest challenges facing neuro-oncologists and radiologists treating patients with brain tumours is diffuse tumour cell infiltration and vascular co-option. In these regions the BBB remains intact, precluding detection by conventional Gd-DTPA-enhanced MRI. We therefore used multiparametric MRI, incorporating both Gd-DTPA and USPIO particle contrast agents, coupled with histogram and unsupervised cluster analyses, to evaluate the additional information that can be obtained regarding the underlying biology of intracranial tumours when the data acquired from sequences assessing tumour vascular permeability, blood volume and water diffusion are combined (18).

A key issue at the outset of this study was the application of our multiparametric MRI strategy in intracranial tumour models displaying a clinically relevant invasive phenotype. RG2 rat glioma cells had previously been shown to display an infiltrative growth pattern and very limited extravasation of Gd-DTPA when propagated intracranially in mice (26). In our experience however, RG2 tumours consistently grew as relatively well circumscribed masses with limited local invasion that demonstrated signal enhancement following administration of Gd-DTPA, a phenotype consistent with the reported morphology of RG2 tumours grown in syngeneic Fischer 344 rats (27,28). Intracranial tumours derived from MDA-MB-231 LM2-4 cells, isolated from a lung metastasis following orthotopic implantation of MDA-MB-231 cells (10), which grow in a partially expansive, partially invasive manner (13) were therefore included in this study as a model of

invasive tumour growth in the brain. Intracranial injection of parental MDA-MB-231 cells has also been used to provide a model of metastatic brain disease (29).

Interesting differences were apparent in the vascular phenotypes of the two tumour models studied. MDA-MB-231 LM2-4 tumours demonstrated higher ΔR_1 than RG2 tumours, indicative of a higher degree of extravasation of contrast agent, hence more permeable vasculature. However, their fBV was lower than that of RG2 tumours, suggesting that, in the simplest terms, high vascular permeability does not necessarily correspond with high vascular density. Cluster analysis of fBV and ΔR_1 allowed for these regions to be mapped spatially; those with low vascular density, but high vascular permeability (Figure 3b, yellow on ΔR_1/fBV map, red on 3D cluster map), are likely indicative of regions of vasculogenesis, where sparse, immature permeable vessels are sprouting to provide a nutritive blood supply to the surrounding tumour cells (30). As expected, these regions were typically found within the principal tumour mass. Areas with low vascular volume and low vascular permeability (Figure 3b, red on ΔR_1/fBV map) include those vessels that are not perfused, but may also correspond to areas with a low density of mature, relatively impermeable vessels, likely areas where the native vessels have been co-opted in regions of invasion (31). Indeed, these voxels, particularly in the MDA-MB-231 LM2-4 tumours, were predominantly located at the tumour margin, where tumour cell invasion was identified on H&E stained sections. Regions with high fBV had either more densely packed or larger calibre vessels, resulting in a relatively larger blood volume. Regions where both parameters were high, which only formed a separate cluster in the RG2 tumours (green), likely correspond to regions with either extensive neovasculature or large distended vessels (32).

MRI protocols incorporating two vascular contrast agents, either an iron oxide preparation in combination with a gadolinium-based agent, or sequential injection of low and then high molecular weight gadolinium-based agents, performed either in the same imaging session or separated by

hours, have previously been used to assess tumour vasculature in intracranial tumour models in rats and mice (33-37), and for assessing response to anti-angiogenic treatment in melanoma xenografts in mice (38). The key advantage of the imaging strategy used herein is that it enabled the spatial analysis of how the vascular biomarkers assessed by the different contrast agents relate to each other, providing further insight into vascular phenotype and heterogeneity.

Iron oxide based contrast agents such as P904 have been used extensively pre-clinically to assess tumour vascular architecture and function (39), but, to date, no iron oxide preparation has been approved for vascular imaging of patients with cancer. Recent studies have highlighted the off-label use of ferumoxytol (Feraheme®), an iron replacement therapy for patients with anaemia, as an intravenous MRI contrast agent (40). A number of clinical trials are underway, including the assessment of tumour vasculature in combination with gadolinium-based contrast agents in the same imaging session in adults with primary brain cancer or brain metastases, and in children with brain tumours (41). Studies such as these, which incorporate methods similar to those used in this study, may guide the creation of new imaging criteria/biomarkers to evaluate brain tumour progression and pseudo-progression secondary to radio-chemotherapy and anti-angiogenic agents.

Susceptibility contrast MRI exploits negative contrast induced by USPIO particles, which inherently reduce signal-to-noise ratios (SNR). The Bayesian maximum *a posteriori* model used herein provides a thorough treatment of data point estimates of R_2* involving representation of the associated uncertainties. For susceptibility contrast MRI it allows the determination of the significance of differences in R_2* between two or more measurements, and consequently the probability that ΔR_2* is greater than or less than zero on a pixel-by-pixel basis *in vivo* can be estimated (14). This method represents a more stringent calculation of MRI parameters when SNR is modest or low. Susceptibility artefacts as a result of the air-tissue interface can emerge in MGE images, but any data affected by such artefacts was excluded from analysis in this study.

We were interested to find that, whilst susceptibility contrast MRI–derived measurements of tumour fBV have previously been validated against uptake of the perfusion marker Hoechst 33342 (42) and a similar correlation was determined in the RG2 model herein, no such significant relationship was determined in the more invasive MDA-MB-231 LM2-4 tumours. We are pursuing further investigations into the pathological assessment of functional vasculature in invasive tumour models in order to understand this relationship more clearly.

In addition to the assessment of tumour vasculature in the brain, the ability to assess cell density in brain malignancies using diffusion-weighted MRI is crucial, particularly where the permeability of the BBB is low. However, care must taken when interpreting ADC measurements, as the relationship between ADC and cell density can be complex, with relatively unrestricted diffusion in areas of oedema and necrosis offset by the reduced ADC in areas of increased cell density. Whilst neither model assessed in this study demonstrated significant necrosis, MDA-MB-231 LM2-4 tumours demonstrated evidence of oedema and lower cell density compared to RG2 tumours. This was reflected in higher ADC and native T_1 and T_2 relaxation times, measures of the ratio of bound to free water in a tissue, reflecting increased extracellular space in the tumours (43). Histogram analysis of the distribution of ADC values further highlighted differences between tumour types, and compared with uninvolved regions of the brain. ADC values over $900x10^{-6}mm^2s^{-1}$ were rare in uninvolved brain regions, uncommon in RG2 tumours, but made up a significant proportion of MDA-MB-231 LM2-4 tumour voxels. These high ADC values represent the relatively unrestricted water diffusion in the areas of oedema observed on H&E stained MDA-MB-231 LM2-4 tumour sections that are absent from RG2 tumours. RG2 tumours were also more cellularly dense, consistent with the higher proportion of pixels with low ADC values (44). Interestingly, despite high cellular density and no oedema or necrosis, RG2 tumours had median ADC values and data distributions higher than the uninvolved brain. Assessment of cluster maps of MDA-MB-231 LM2-

4 tumours incorporating ADC data, alongside H&E staining of the same tumours, revealed clusters of particular note driven by high ADC, denoting relatively unrestricted diffusion. These voxels displayed low ΔR_1 and fBV (low vascular permeability and vascular volume) (Figure 3b, yellow cluster on all 2D and 3D maps including ADC), and corresponded to histologically confirmed regions of invasive tumour growth associated with oedema. A key imaging hallmark of brain tumours is an area of fluid-attenuated inversion recovery (FLAIR) or T_2-weighted MRI hyperintensity outside the region of contrast enhancement, consisting of a combination of infiltrating tumour cells and oedema (45). The routine incorporation of diffusion-weighted imaging to gadolinium-enhanced imaging protocols in the clinic may thus assist in the more accurate resolution and characterisation of these brain tumour regions (46).

Multiparametric MRI, focussing particularly on the microvasculature, was used by Coquery *et al.* to establish MRI-derived clusters to characterise tumour heterogeneity, and correlated them to pathophysiological features, in rat brain tumour models (25).

MRI-based brain tumour segmentation to separate different tumour subcompartments from normal brain structures has been largely performed using supervised learning techniques, which are time consuming and expensive due to the requirement of teaching datasets and labelled images (47). Unsupervised methods are now increasingly being developed and have been shown to perform well in comparison to supervised techniques (24). Of particular importance is the segmentation of non-enhancing tumour from healthy tissue to monitor tumour size more accurately over time (48).

Further refinements in these techniques include 3D histogram analysis of routinely acquired images to identify radiologically-defined regional habitat variations in brain tumour data to provide deeper insight into the evolutionary dynamics of brain tumours (22), and the incorporation of quantitative functional parameters such as diffusion tensor imaging (DTI) and dynamic susceptibility contrast (DSC) MRI into machine learning algorithms, which identified complex and reproducible imaging patterns predictive of overall survival and molecular subtypes in glioblastoma (23).

In summary, intracranial implantation of MDA-MB-231 LM2-4 cells provides a useful model for the development of imaging biomarkers of the vascular and invasive phenotypes of tumours in the brain. We have demonstrated that multiparametric MRI, coupled with unsupervised cluster analysis, allows assessment of the patency of tumour vasculature by simultaneous assessment of both vascular permeability and tumour blood volume, potentially allowing delineation of vasculogenic regions and regions of co-opted normal brain vasculature. Spatial assessment of tissue diffusion properties in combination with vascular characteristics enabled the relationship between oedema and invasion/vascular co-option to be evaluated. Development and translation of such techniques that strengthen the links between *in vivo* imaging biomarkers and the structural and functional properties of tissue has the potential to provide predictive models to improve brain tumour diagnosis, prognosis and monitoring.

Acknowledgments

We thank Allan Thornhill and his staff for animal maintenance and Philippe Robert at Guerbet for supplying P904®.

Figure Legends

Figure 1

a) T_2-weighted MRI images and parametric maps of native T_1 and T_2 relaxation times, apparent diffusion coefficient (ADC), the change in relaxation rate R_1 following intravenous administration of Gd-DTPA (ΔR_1), and fractional blood volume (fBV), from representative RG2 (upper panels) and MDA-MB-231 LM2-4 (lower panels) tumours propagated in the brain. **b)** Frequency histograms displaying the distribution of ADC, ΔR_1 and fBV in RG2 and MDA-MB-231 LM2-4 tumours, and uninvolved brain tissue (data from all evaluated ROIs). Sufficient data could not be acquired from matched uninvolved brain tissue for ΔR_1 analysis, therefore values from brain tissue in tumour bearing mice where data could be assessed were combined (uninvolved).

Figure 2

a) Haematoxylin and eosin (H&E) staining of RG2 and MDA-MB-231 LM2-4; whole brain composite images and 100x images of the tumour periphery (middle panel) showed RG2 tumours as relatively well circumscribed masses with some local invasion at the periphery, and MDA-MB-231 LM2-4 tumours as substantially locally invasive (open head arrow shows tumour cells surrounding a blood vessel) with associated oedema (closed head arrow). Right panel shows cell density at the centre of the tumours. Mean cellular density was assessed in both tumour types; MDA-MB-231 LM2-4 tumours were significantly less dense. **b)** Fluorescence microscopy of Hoechst 33342 uptake in representative RG2 and MDA-MB-231 LM2-4 tumour bearing brains revealed no significant difference between the perfused areas in the two tumour types. *$p<0.05$, unpaired Student's t-test.

Figure 3

a) Cumulative distribution of voxels in the bi- or tri-dimensional space formed by two or three analysed parameters. Delta R_1 (ΔR_1) and fractional blood volume (fBV) in RG2; ΔR_1 and fBV, ΔR_1

and apparent diffusion coefficient (ADC), fBV and ADC, and all three parameters in MDA-MB-231 LM2-4 tumours. ΔR_1 is expressed in units of $x10\text{-}^{6}ms^{-1}$, fBV in %, and ADC in units of $\times 10^{-6}mm^{2}s^{-1}$. 2D projections of the clustered 3D voxel distribution are shown in Figure S1b. **b)** Corresponding cluster analysis maps of RG2 and MDA-MB-231 LM2-4 tumours; where data thresholding was applied, these values are removed from the maps. Voxels without an evaluable fBV (negative ΔR_2*) are also missing from analyses incorporating fBV. **c)** H&E staining of the same tumours shows spatial relationships between cluster analysis maps and the tumour physiology. Closed head arrow denotes region of invasion along blood vessels and oedema, open head arrow denotes invasion without oedema, dashed arrow denotes main dense tumour mass.

References

1. Ostrom QT, Gittleman H, Liao P, Rouse C, Chen Y, Dowling J, Wolinsky Y, Kruchko C, Barnholtz-Sloan J. CBTRUS Statistical Report: Primary Brain and Central Nervous System Tumors Diagnosed in the United States in 2007–2011. *Neuro Oncol.* 2014;**16**:iv1-iv63.

2. Schouten LJ, Rutten J, Huveneers HA, Twijnstra A. Incidence of brain metastases in a cohort of patients with carcinoma of the breast, colon, kidney, and lung and melanoma. *Cancer.* 2002;**94**:2698-2705.

3. Arshad F, Wang L, Sy C, Avraham S, Avraham HK. Blood-brain barrier integrity and breast cancer metastasis to the brain. *Patholog Res Int.* 2010;**2011**:920509.

4. Giese A, Westphal M. Glioma invasion in the central nervous system. *Neurosurgery.* 1996;**39**:235-250; discussion 250-232.

5. Rees J. Advances in magnetic resonance imaging of brain tumours. *Curr Opin Neurol.* 2003;**16**:643-650.

6. O'Connor JP, Rose CJ, Waterton JC, Carano RA, Parker GJ, Jackson A. Imaging intratumor heterogeneity: role in therapy response, resistance, and clinical outcome. *Clin Cancer Res.* 2015;**21**:249-257.

7. Walker-Samuel S, Boult JK, McPhail LD, Box G, Eccles SA, Robinson SP. Non-invasive in vivo imaging of vessel calibre in orthotopic prostate tumour xenografts. *Int J Cancer.* 2012;**130**:1284-1293.

8. Just N. Histogram analysis of the microvasculature of intracerebral human and murine glioma xenografts. *Magn Reson Med.* 2011;**65**:778-789.

9. Lemasson B, Valable S, Farion R, Krainik A, Remy C, Barbier EL. In vivo imaging of vessel diameter, size, and density: a comparative study between MRI and histology. *Magn Reson Med.* 2013;**69**:18-26.

10. Munoz R, Man S, Shaked Y, Lee CR, Wong J, Francia G, Kerbel RS. Highly efficacious nontoxic preclinical treatment for advanced metastatic breast cancer using combination oral UFT-cyclophosphamide metronomic chemotherapy. *Cancer Res.* 2006;**66**:3386-3391.

11. Workman P, Aboagye E, Balkwill F, Balmain A, Bruder G, Chaplin D, Double J, Everitt J, Farningham D, Glennie M, Kelland L, Robinson V, Stratford I, Tozer G, Watson S, Wedge S, Eccles S, Navaratnam V, Ryder S, Institute CotNCR. Guidelines for the welfare and use of animals in cancer research. *Br J Cancer.* 2010;**102**:1555-1577.

12. Kilkenny C, Browne WJ, Cuthill IC, Emerson M, Altman DG. Improving bioscience research reporting: the ARRIVE guidelines for reporting animal research. *PLoS Biol.* 2010;**8**:e1000412.

13. Jamin Y, Boult JK, Li J, Popov S, Garteiser P, Ulloa JL, Cummings C, Box G, Eccles SA, Jones C, Waterton JC, Bamber JC, Sinkus R, Robinson SP. Exploring the biomechanical properties of brain malignancies and their pathologic determinants in vivo with magnetic resonance elastography. *Cancer Res.* 2015;**75**:1216-1224.

14. Walker-Samuel S, Orton M, McPhail LD, Boult JK, Box G, Eccles SA, Robinson SP. Bayesian estimation of changes in transverse relaxation rates. *Magn Reson Med.* 2010;**64**:914-921.

15. Walker-Samuel S, Orton M, Boult JK, Robinson SP. Improving apparent diffusion coefficient estimates and elucidating tumor heterogeneity using Bayesian adaptive smoothing. *Magn Reson Med.* 2011;**65**:438-447.

16. Tropres I, Grimault S, Vaeth A, Grillon E, Julien C, Payen JF, Lamalle L, Decorps M. Vessel size imaging. *Magn Reson Med.* 2001;**45**:397-408.

17. Troprès I, Lamalle L, Péoc'h M, Farion R, Usson Y, Décorps M, Rémy C. In vivo assessment of tumoral angiogenesis. *Magn Reson Med.* 2004;**51**:533-541.

18. Borri M, Schmidt MA, Powell C, Koh DM, Riddell AM, Partridge M, Bhide SA, Nutting CM, Harrington KJ, Newbold KL, Leach MO. Characterizing Heterogeneity within Head and Neck Lesions Using Cluster Analysis of Multi-Parametric MRI Data. *PLoS One.* 2015;**10**:e0138545.

19. Sugar CA, James GM. Finding the number of clusters in a dataset: An information-theoretic approach. *J Am Statist Assoc.* 2003;**98**:750-763.

20. Boult JK, Walker-Samuel S, Jamin Y, Leiper JM, Whitley GS, Robinson SP. Active site mutant dimethylarginine dimethylaminohydrolase 1 expression confers an intermediate tumour phenotype in C6 gliomas. *The Journal of pathology.* 2011;**225**:344-352.

21. Schnapauff D, Zeile M, Niederhagen MB, Fleige B, Tunn PU, Hamm B, Dudeck O. Diffusion-weighted echo-planar magnetic resonance imaging for the assessment of tumor cellularity in patients with soft-tissue sarcomas. *J Magn Reson Imaging.* 2009;**29**:1355-1359.

22. Zhou M, Hall L, Goldgof D, Russo R, Balagurunathan Y, Gillies R, Gatenby R. Radiologically defined ecological dynamics and clinical outcomes in glioblastoma multiforme: preliminary results. *Transl Oncol.* 2014;**7**:5-13.

23. Macyszyn L, Akbari H, Pisapia JM, Da X, Attiah M, Pigrish V, Bi Y, Pal S, Davuluri RV, Roccograndi L, Dahmane N, Martinez-Lage M, Biros G, Wolf RL, Bilello M, O'Rourke DM, Davatzikos C. Imaging patterns predict patient survival and molecular subtype in glioblastoma via machine learning techniques. *Neuro Oncol.* 2016;**18**:417-425.

24. Juan-Albarracin J, Fuster-Garcia E, Manjon JV, Robles M, Aparici F, Marti-Bonmati L, Garcia-Gomez JM. Automated glioblastoma segmentation based on a multiparametric structured unsupervised classification. *PLoS One.* 2015;**10**:e0125143.

25. Coquery N, Francois O, Lemasson B, Debacker C, Farion R, Remy C, Barbier EL. Microvascular MRI and unsupervised clustering yields histology-resembling images in two rat models of glioma. *J Cereb Blood Flow Metab.* 2014;**34**:1354-1362.

26. Kemper EM, Leenders W, Kusters B, Lyons S, Buckle T, Heerschap A, Boogerd W, Beijnen JH, van Tellingen O. Development of luciferase tagged brain tumour models in mice for chemotherapy intervention studies. *Eur J Cancer.* 2006;**42**:3294-3303.

27. Doblas S, He T, Saunders D, Pearson J, Hoyle J, Smith N, Lerner M, Towner RA. Glioma morphology and tumor-induced vascular alterations revealed in seven rodent glioma models by in vivo magnetic resonance imaging and angiography. *J Magn Reson Imaging.* 2010;**32**:267-275.

28. Valable S, Lemasson B, Farion R, Beaumont M, Segebarth C, Remy C, Barbier EL. Assessment of blood volume, vessel size, and the expression of angiogenic factors in two rat glioma models: a longitudinal in vivo and ex vivo study. *NMR Biomed.* 2008;**21**:1043-1056.

29. Kim B, Kim K, Im KH, Kim JH, Lee JH, Jeon P, Byun H. Multiparametric MR imaging of tumor response to intraarterial chemotherapy in orthotopic xenograft models of human metastatic brain tumor. *J Neurooncol.* 2016;**127**:243-251.

30. Dvorak HF, Nagy JA, Feng D, Brown LF, Dvorak AM. Vascular permeability factor/vascular endothelial growth factor and the significance of microvascular hyperpermeability in angiogenesis. *Curr Top Microbiol Immunol.* 1999;**237**:97-132.

31. Leenders WP, Kusters B, de Waal RM. Vessel co-option: how tumors obtain blood supply in the absence of sprouting angiogenesis. *Endothelium.* 2002;**9**:83-87.

32. Yuan F, Salehi HA, Boucher Y, Vasthare US, Tuma RF, Jain RK. Vascular permeability and microcirculation of gliomas and mammary carcinomas transplanted in rat and mouse cranial windows. *Cancer Res.* 1994;**54**:4564-4568.

33. Beaumont M, Lemasson B, Farion R, Segebarth C, Remy C, Barbier EL. Characterization of tumor angiogenesis in rat brain using iron-based vessel size index MRI in combination with gadolinium-based dynamic contrast-enhanced MRI. *J Cereb Blood Flow Metab.* 2009;**29**:1714-1726.

34. Pannetier N, Lemasson B, Christen T, Tachrount M, Tropres I, Farion R, Segebarth C, Remy C, Barbier EL. Vessel size index measurements in a rat model of glioma: comparison of the dynamic

(Gd) and steady-state (iron-oxide) susceptibility contrast MRI approaches. *NMR Biomed.* 2012;**25**:218-226.

35. Pike MM, Stoops CN, Langford CP, Akella NS, Nabors LB, Gillespie GY. High-resolution longitudinal assessment of flow and permeability in mouse glioma vasculature: Sequential small molecule and SPIO dynamic contrast agent MRI. *Magn Reson Med.* 2009;**61**:615-625.

36. Gambarota G, Leenders W, Maass C, Wesseling P, van der Kogel B, van Tellingen O, Heerschap A. Characterisation of tumour vasculature in mouse brain by USPIO contrast-enhanced MRI. *Br J Cancer.* 2008;**98**:1784-1789.

37. Lemasson B, Serduc R, Maisin C, Bouchet A, Coquery N, Robert P, Le Duc G, Tropres I, Remy C, Barbier EL. Monitoring blood-brain barrier status in a rat model of glioma receiving therapy: dual injection of low-molecular-weight and macromolecular MR contrast media. *Radiology.* 2010;**257**:342-352.

38. Rudin M, McSheehy PM, Allegrini PR, Rausch M, Baumann D, Becquet M, Brecht K, Brueggen J, Ferretti S, Schaeffer F, Schnell C, Wood J. PTK787/ZK222584, a tyrosine kinase inhibitor of vascular endothelial growth factor receptor, reduces uptake of the contrast agent GdDOTA by murine orthotopic B16/BL6 melanoma tumours and inhibits their growth in vivo. *NMR Biomed.* 2005;**18**:308-321.

39. Tropres I, Pannetier N, Grand S, Lemasson B, Moisan A, Peoc'h M, Remy C, Barbier EL. Imaging the microvessel caliber and density: Principles and applications of microvascular MRI. *Magn Reson Med.* 2014;DOI: 10.1002/mrm.25396.

40. Bashir MR, Bhatti L, Marin D, Nelson RC. Emerging applications for ferumoxytol as a contrast agent in MRI. *J Magn Reson Imaging.* 2015;**41**:884-898.

41. ClinicalTrials.gov. https://clinicaltrials.gov/ct2/results?term=ferumoxytol&Search=Search. Health USNIo. 20th March 2015

42. Robinson S, Howe F, Griffiths J, Ryan A, Waterton J. Susceptibility contrast magnetic resonance imaging determination of fractional tumor blood volume: a noninvasive imaging biomarker of response to the vascular disrupting agent ZD6126. *Int J Radiat Oncol Biol Phys.* 2007;**69**:872-879.

43. Jakobsen I, Lyng H, Kaalhus O, Rofstad E. MRI of human tumor xenografts in vivo: proton relaxation times and extracellular tumor volume. *Magn Reson Imaging.* 1995;**13**:693-700.

44. Chen L, Liu M, Bao J, Xia Y, Zhang J, Zhang L, Huang X, Wang J. The correlation between apparent diffusion coefficient and tumor cellularity in patients: a meta-analysis. *PLoS One.* 2013;**8**:e79008.

45. Kelly PJ, Daumas-Duport C, Kispert DB, Kall BA, Scheithauer BW, Illig JJ. Imaging-based stereotaxic serial biopsies in untreated intracranial glial neoplasms. *J Neurosurg.* 1987;**66**:865-874.

46. Pavlisa G, Rados M, Pavlisa G, Pavic L, Potocki K, Mayer D. The differences of water diffusion between brain tissue infiltrated by tumor and peritumoral vasogenic edema. *Clin Imaging.* 2009;**33**:96-101.

47. Gordillo N, Montseny E, Sobrevilla P. State of the art survey on MRI brain tumor segmentation. *Magn Reson Imaging.* 2013;**31**:1426-1438.

48. Fletcher-Heath LM, Hall LO, Goldgof DB, Murtagh FR. Automatic segmentation of non-enhancing brain tumors in magnetic resonance images. *Artif Intell Med.* 2001;**21**:43-63.

	RG2	MDA-MB-231 LM2-4	RG2 uninvolved *(n=6)*	MDA-MB-231 LM2-4 uninvolved *(n=7)*	Uninvolved *(n=3)*
T_1 (ms)	1278 ± 12 (*n=5)*	1402 ± 18 *** (*n=7)*	-	-	1227 ± 25 §§§
T_2 (ms)	48.3 ± 1.3 (*n=5)*	58.3 ± 2.5 * (*n=7)*	-	-	41.9 ± 2.1 * §§
ADC ($x10^{-6}mm^2s^{-1}$)	644 ± 16 (*n=10)*	811 ± 27 *** (*n=8)*	585 ± 9 $^{\#}$	576 ± 23 $^{\#\#\#\#}$	-
ΔR_1 ($x10^{-6}ms^{-1}$)	246 ± 49 (*n=5)*	420 ± 46 * (*n=6)*	-	-	41 ± 8 * §§
$fBV_{<17}$ (%)	6.8 ± 0.2 (*n=13)*	5.8 ± 0.3 ** (*n=8)*	4.0 ± 0.2 $^{\#\#\#\#}$	4.4 ± 0.5 $^{\#}$	-

Table 1. Summary of the quantitative native and contrast-enhanced MRI biomarkers acquired in intracranially propagated RG2 and MDA-MB-231LM2-4 tumours and uninvolved regions of tumour bearing brains.

T_1 = longitudinal relaxation time, T_2 = transverse relaxation time, ADC = apparent diffusion coefficient, ΔR_1 = change in the longitudinal relaxation rate R_1 following intravenous administration of Gd-DTPA, $fBV_{<17}$ = fractional blood volume with an upper threshold of 17%. Data are mean of median parameter values from each tumour. * $p<0.05$, ** $p<0.01$, *** $p<0.001$ vs RG2; §§ $p<0.01$, §§§ $p<0.001$, Student's unpaired t-test; $^{\#}$ $p<0.05$, $^{\#\#\#\#}$ $p<0.0001$ vs matched tumour ROIs, Student's paired t-test.

Figure 1

a

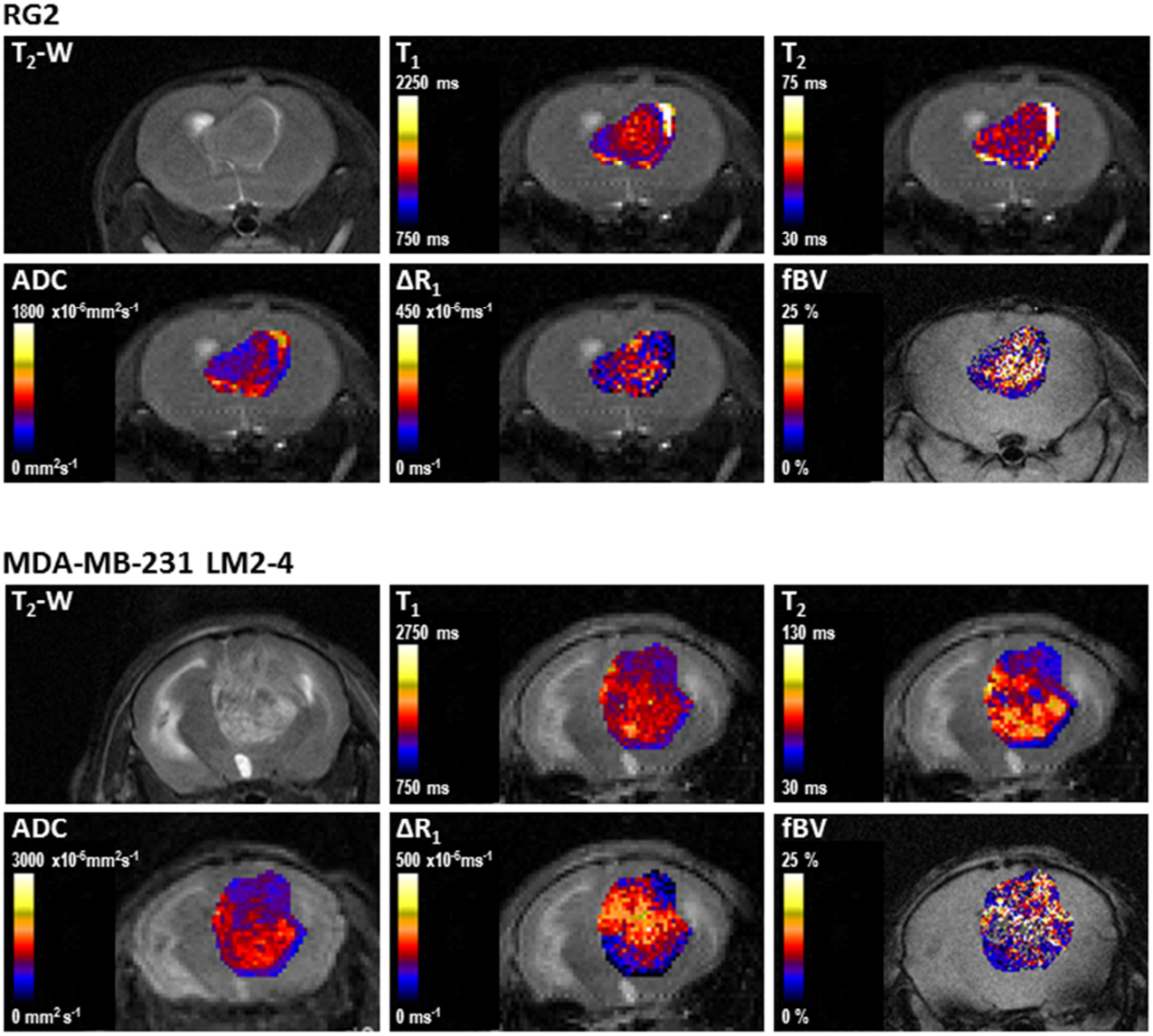
RG2
T2-W
T1
2250 ms
750 ms
T2
75 ms
30 ms
ADC
1800 x10-6mm2s-1
0 mm2s-1
ΔR1
450 x10-6ms-1
0 ms-1
fBV
25 %
0 %
MDA-MB-231 LM2-4
T2-W
T1
2750 ms
750 ms
T2
130 ms
30 ms
ADC
3000 x10-6mm2s-1
0 mm2 s-1
ΔR1
500 x10-6ms-1
0 ms-1
fBV
25 %
0 %

b

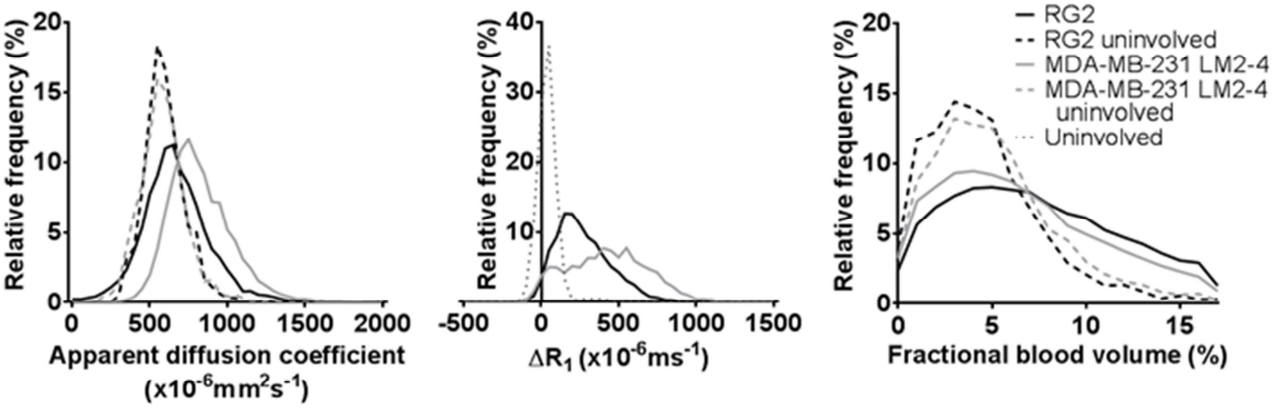
Relative frequency (%)
Apparent diffusion coefficient (x10-6mm2s-1)
ΔR1 (x10-6ms-1)
Fractional blood volume (%)
RG2
RG2 uninvolved
MDA-MB-231 LM2-4
MDA-MB-231 LM2-4 uninvolved
Uninvolved

Figure 2

a

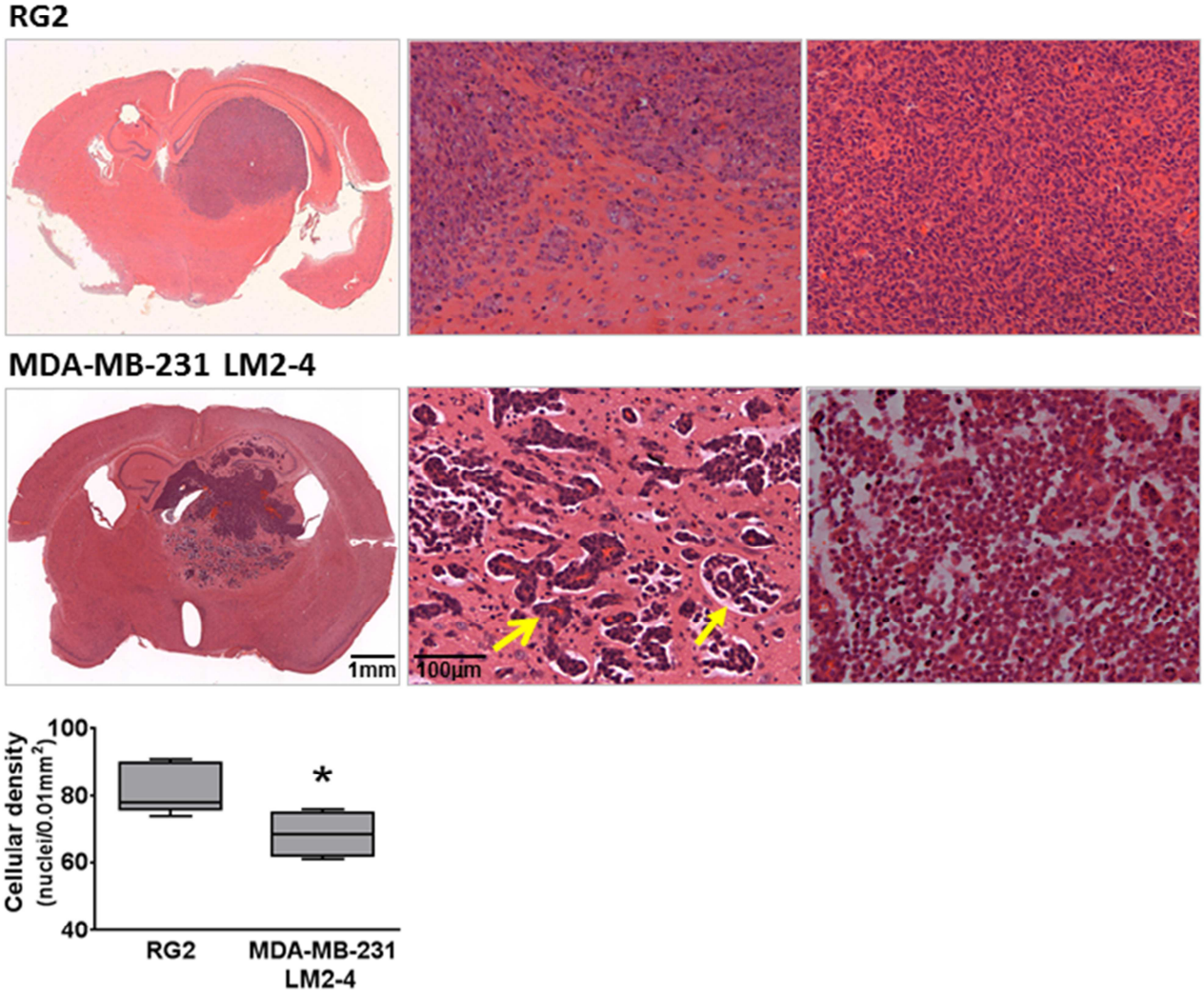
RG2
MDA-MB-231 LM2-4
1mm
100µm
Cellular density (nuclei/0.01mm²)
100
80
60
40
*
RG2
MDA-MB-231 LM2-4

b

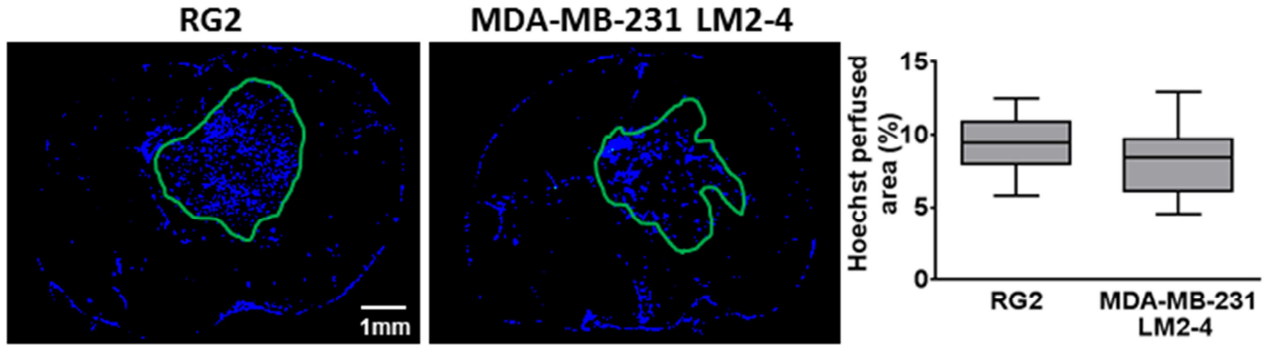
RG2
MDA-MB-231 LM2-4
1mm
Hoechst perfused area (%)
15
10
5
0
RG2
MDA-MB-231 LM2-4

Figure 3

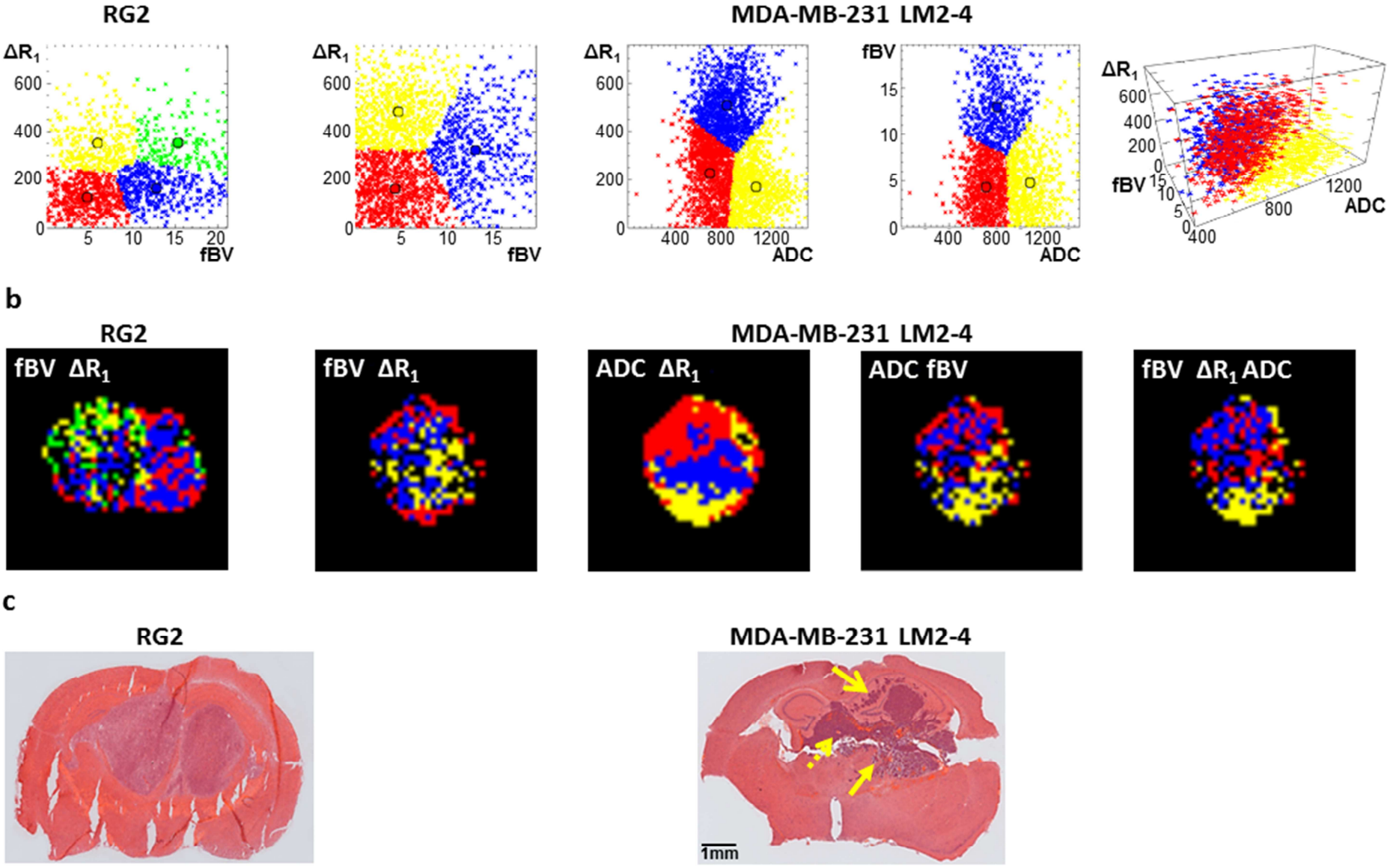
a
RG2
MDA-MB-231 LM2-4
ΔR1
fBV
ADC
b
RG2
MDA-MB-231 LM2-4
fBV ΔR1
fBV ΔR1
ADC ΔR1
ADC fBV
fBV ΔR1 ADC
c
RG2
MDA-MB-231 LM2-4
1mm

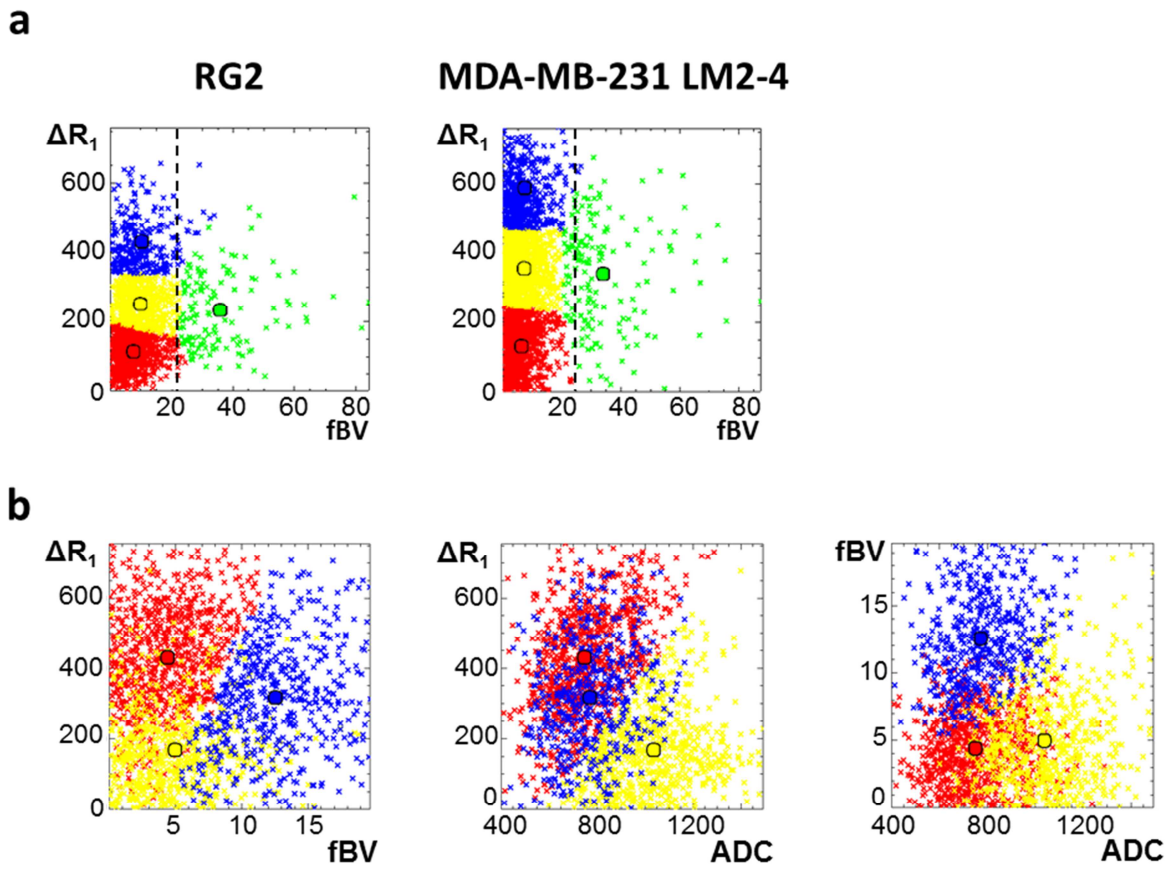

Supplementary Figure S1

a) Cumulative distribution of voxels in the bi-dimensional space formed by delta R_1 (ΔR_1, $x10^{-6}ms^{-1}$) and fractional blood volume (fBV, %) in RG2 and MDA-MB-231 LM2-4 without an upper threshold, showing the cluster distribution dominated by and 'outlier cluster of high fBV values. Dashed line denotes threshold set as value at which a datapoint has only a 5% probability of belonging to the 'outlier' cluster. **b)** 2D projections of the clustered 3D voxel distribution of ΔR1, fBV, and ADC in MDA-MB-231 LM2-4 (Figure 3a), providing a 2D view of the distribution for each parameter pair.